



AFRL-OSR-VA-TR-2014-0249

THERMAL REGULATION OF HEAT TRANSFER PROCESSES

GANG CHEN
MASSACHUSETTS INSTITUTE OF TECHNOLOGY

10/02/2014
Final Report

DISTRIBUTION A: Distribution approved for public release.

Air Force Research Laboratory
AF Office Of Scientific Research (AFOSR)/ RTB
Arlington, Virginia 22203
Air Force Materiel Command

REPORT DOCUMENTATION PAGE				<i>Form Approved</i> <i>OMB No. 0704-0188</i>	
<small>Public reporting burden for this collection of information is estimated to average 1 hour per response, including the time for reviewing instructions, searching existing data sources, gathering and maintaining the data needed, and completing and reviewing this collection of information. Send comments regarding this burden estimate or any other aspect of this collection of information, including suggestions for reducing this burden to Department of Defense, Washington Headquarters Services, Directorate for Information Operations and Reports (0704-0188), 1215 Jefferson Davis Highway, Suite 1204, Arlington, VA 22202-4302. Respondents should be aware that notwithstanding any other provision of law, no person shall be subject to any penalty for failing to comply with a collection of information if it does not display a currently valid OMB control number. PLEASE DO NOT RETURN YOUR FORM TO THE ABOVE ADDRESS.</small>					
1. REPORT DATE (DD-MM-YYYY)		2. REPORT TYPE		3. DATES COVERED (From - To)	
4. TITLE AND SUBTITLE				5a. CONTRACT NUMBER	
				5b. GRANT NUMBER	
				5c. PROGRAM ELEMENT NUMBER	
6. AUTHOR(S)				5d. PROJECT NUMBER	
				5e. TASK NUMBER	
				5f. WORK UNIT NUMBER	
7. PERFORMING ORGANIZATION NAME(S) AND ADDRESS(ES)				8. PERFORMING ORGANIZATION REPORT NUMBER	
9. SPONSORING / MONITORING AGENCY NAME(S) AND ADDRESS(ES)				10. SPONSOR/MONITOR'S ACRONYM(S)	
				11. SPONSOR/MONITOR'S REPORT NUMBER(S)	
12. DISTRIBUTION / AVAILABILITY STATEMENT					
13. SUPPLEMENTARY NOTES					
14. ABSTRACT					
15. SUBJECT TERMS					
16. SECURITY CLASSIFICATION OF:			17. LIMITATION OF ABSTRACT	18. NUMBER OF PAGES	19a. NAME OF RESPONSIBLE PERSON
a. REPORT	b. ABSTRACT	c. THIS PAGE			19b. TELEPHONE NUMBER (include area code)

THERMAL REGULATION OF HEAT TRANSFER PROCESSES

Principal Investigator: Gang Chen

Department of Mechanical Engineering

Massachusetts Institute of Technology

Cambridge, MA 02139

This project aims at developing scientific underpinnings to tune thermal, electrical, and optical properties of materials. The project focuses on studying fundamental transport processes that determine the contrasts of thermophysical properties of composites and thin films, and various approaches to regulate heat transport processes. In the past three years, multiple methods to regulate heat transport has been studied: **1)** thermal regulation of thermal and electrical conductivity in nanofluids, **2)** thermal regulation of optical properties in thin film, and **3)** thermal regulation of phase transition for efficient steam generation. Besides thermal regulation, we also develop an electrochemical method to regulate thermal conductivity in battery materials. Both experiments and modeling have been carried out in to advance the fundamental understanding of transport processes during switching of thermophysical properties. In the following, progresses in these fields will be reported in details.

1. Thermal regulation of physical properties in nanofluid

Prior to the initiation of the project, we have successfully demonstrated regulations of electrical and thermal conductivity in nanofluid during phase transition¹. The system studied is thin graphite flakes (5-10 nm in thickness, 1-10 μm in size) in hexadecane ($\text{C}_{16}\text{H}_{34}$). The electrical conductivity (EC) and thermal conductivity (TC) increases by a factor of 250 and 3.2, respectively, during the transition from liquid to solid. This effect is attributed to the formation of crystalline grains in solidification, which applies stress to graphite flakes leading to better contact between flakes. In this project, we further studied both effects of conductive phase and host matrix. The effect of conductive phase (e.g. CNTs vs. graphite flakes) will be discussed first, followed by investigation of host matrix (nonpolar eicosane ($\text{C}_{20}\text{H}_{42}$) vs. polar ethylene carbonate ($\text{C}_3\text{H}_4\text{O}_3$)). At last, studies on the viscosity of graphite flake-based nanofluid are presented for better understanding of the system.

1.1 Effect of conductive phase on physical properties of nanofluids

In this study, graphite flakes were replaced by multi-walled carbon nanotubes (CNTs)². Compared to graphite flakes, CNTs are less likely to stick together under repetition of freezing and melting. CNTs are also attractive because of their high EC and TC, remarkable mechanical properties and unique one-dimensional structure. Changes of five orders of magnitude and three times have been observed in EC and TC, respectively, in hexadecane solvent. In contrast, graphite flakes in hexadecane only shows changes of three orders of magnitude in electrical conductivity.

We also find that functionalized CNTs (f-CNTs) induce higher contrast than pure CNTs (p-CNTs). By modifying CNT surface with functional groups, the strong Van der Waals interaction among CNTs can be reduced, which makes CNTs more dispersed and the composite is almost insulating (Fig. 1a). During the freezing of hexadecane, the needle-like hexadecane crystals grow anisotropically (Fig. 1b), and the strong stress generated during the crystals growth forces CNTs to contact with each other and form a conductive percolation network. Hence the composite becomes conductive. When the frozen hexadecane melts again, the pressure on the CNTs is released. The CNTs are separated from each other and re-disperse in the liquid again because of the steric effects of functional groups and liquid convection (Fig. 1c). Such mechanism leads to a high contrast of 10^5 in EC and three times in TC in f-CNTs (Fig. 2a). In contrast, p-CNTs only show a contrast of 10^2 in EC and 2.5 times in TC (Fig. 2b).

Cycling tests also confirms that f-CNTs are more resistive to agglomeration. No obvious change in dispersion are observed between the third and fifteenth cycle for f-CNTs. In contrast, p-CNTs tend to agglomerate under ten to fifteen cycles, which degrades the contrast in electrical and thermal conductivity.

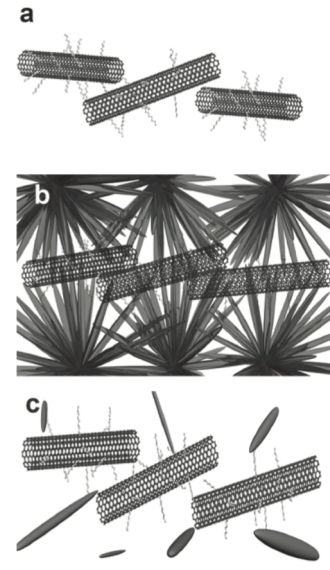


Figure 1. Schematic diagram of the switching process in composite. a) Original state, CNTs are dispersed with the help of surface functional groups. b) Frozen state, CNTs are squeezed to the grain boundary and form a conductive network. c) Remelting, CNTs are re-dispersed in the liquid, and the conductive network is broken.

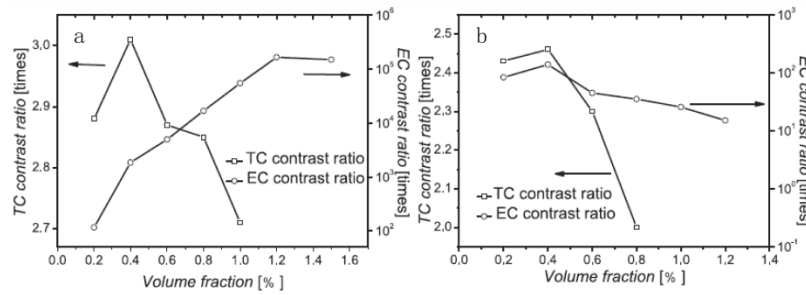


Figure 2. a) Electrical conductivity (EC) and thermal conductivity (TC) contrast ratio of f-MWCNTs/hexadecane composites as a function of volume fraction, the EC and TC contrast ratio

peak at the volume fraction of 1.2% and 0.4%, respectively. b) EC and TC contrast ratio of p-MWCNTs/hexadecane composites as a function of volume fraction, both the EC and TC contrast ratio peak at the volume fraction of 0.4%. All data in the EC and TC switching property tests of the composites are taken after 15 times cycles when the materials stabilize.

1.2 Effect of host materials on physical properties of nanofluids

In our previous studies, hexadecane with a phase transition temperature of 18 °C was used as matrix. However, for many applications (e.g. electrical fuse), it is ideal that the system has a melting point higher than room temperature. We found two types of host materials as our new candidates: eicosane ($C_{20}H_{42}$) with a melting temperature of 36°C, and ethylene carbonate ($C_3H_4O_3$), with a melting temperature of 35-37°C. Although they have very similar melting temperature, their molecular structures and physical properties are significantly different (Fig. 3). Eicosane, non-polar molecule, has similar structure with hexadecane, but with slightly larger molecule size. In contrast, ethylene carbonate is strongly polarized, with a much smaller molecular size than eicosane. As in previous work, graphite flakes prepared by microwave expansion method has been used as the conductive phase in these composites.

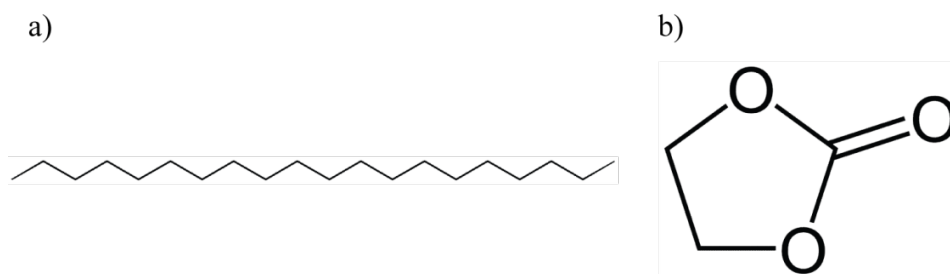


Figure 3. Molecular structure of eicosane and ethylene carbonate. a) eicosane and b) ethylene carbonate.

The electrical conductivities of nanofluids with different solvents were measured first. Eicosane-based nanofluid shows a peak contrast of 200 at 1.0 vol%. In contrast, ethylene carbonate-based nanofluid shows a peak contrast of ~5000 at 1.0 vol%. The electrical conductivity in liquid phases are 10^{-5} and 10^{-7} S cm^{-1} for eicosane and ethylene carbonate-based nanofluid, respectively. Meanwhile, the electrical conductivity in solid phases are 10^{-3} and 10^{-4} S cm^{-1} for eicosane and ethylene carbonate-based nanofluid, respectively. We contribute the difference in solid phase electrical conductivity to different grain structures of two solvents in the solid phase, as shown in Fig. 4a and b. Clearly the aspect ratio of crystal grain in ethylene carbonate is significantly larger than that of eicosane. Moreover, grains in ethylene carbonate are more aligned than that in eicosane, which may result in straighter pathway for electrical conduction.

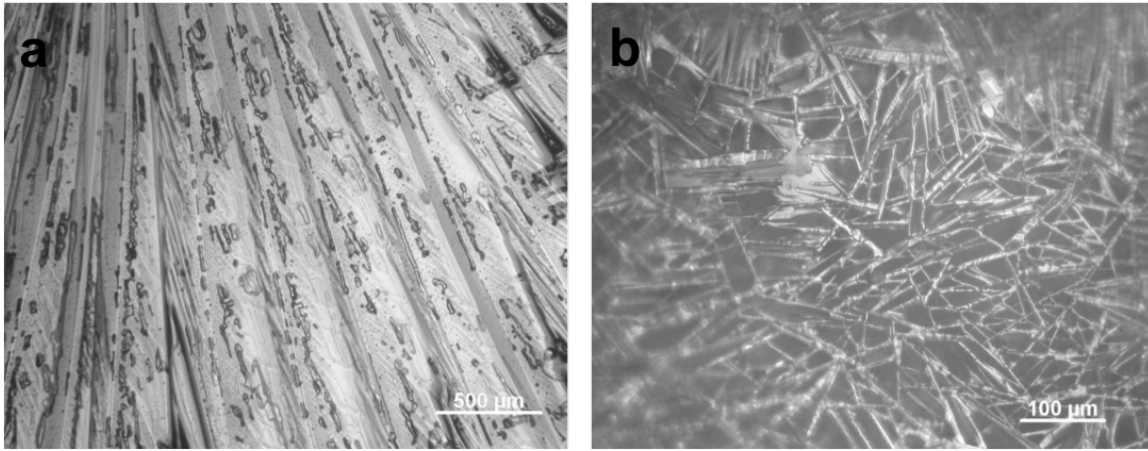


Figure 4. a) Microstructure of Ethylene carbonate crystal. b) Microstructure of Eicosane crystal.

The electrical conductivity contrast observed is stable in cycling, as illustrated in Fig. 5. Typically the first cycle shows the largest electrical conductivity contrast ratio, and the contrast ratio is stabilized afterwards.

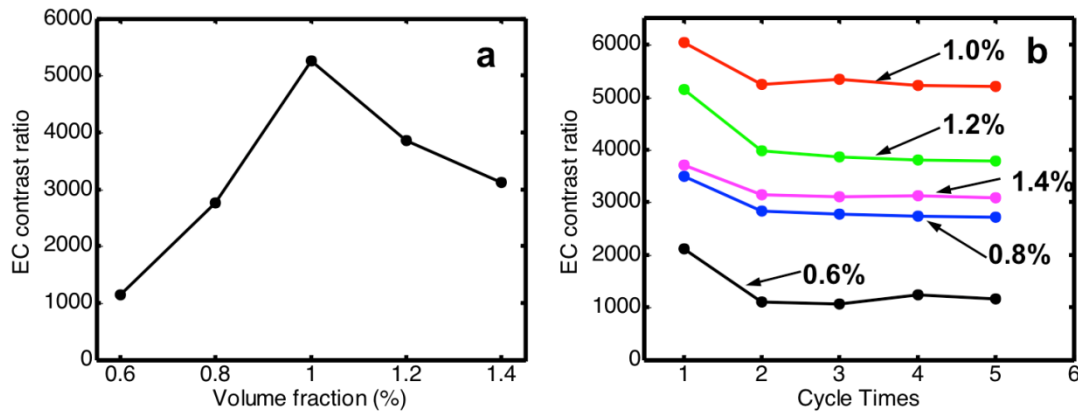


Figure 5. a) Electrical conductivity contrast ratio of graphite flake/ethylene carbonate composites during phase transition as a function of volume fraction. b) Cyclic electrical conductivity contrast ratio of graphite/ethylene carbonate composite during phase transition at different volume fractions (0.6%, 0.8%, 1.0%, 1.2% and 1.4%).

1.3 Viscosity and thermal conductivity of graphite suspensions near percolation

The viscosity of nanofluids and suspensions is another important parameter for practical applications, especially under flowing conditions. For general non-Newtonian fluids, the viscosity is not only a function of temperature, but also a function of the shear rate and shear history. Past work has shown that the viscosity of nanofluids typically decreases with increasing temperature^{3, 4}. Although suspension viscosity has been extensively studied in literatures^{5, 6}, there have been little studies about the temperature effect on suspension viscosity when the volume loading transits from dilute to the percolated regime. We measured the thermal conductivity and viscosity of graphite suspensions as a function of volume fraction in the liquid state, focusing on the percolation behavior⁷. Different trends for thermal conductivity and viscosity are observed below and above percolation (Fig. 6).

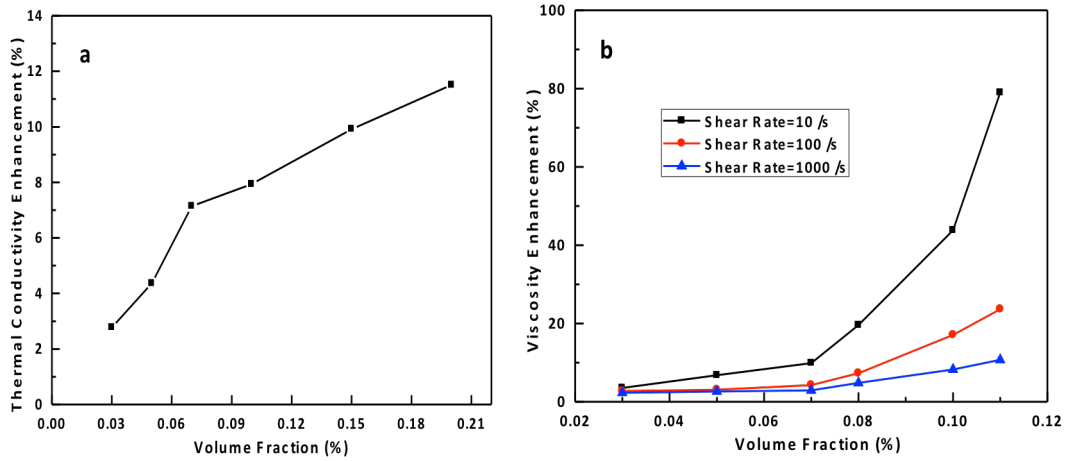


Figure 6: (a) Thermal conductivity enhancement of graphite suspension as a function of volume fraction near the percolation concentration of 0.07% (b) Viscosity enhancement of graphite suspension as a function of volume fraction near the percolation regime at given shear rates.

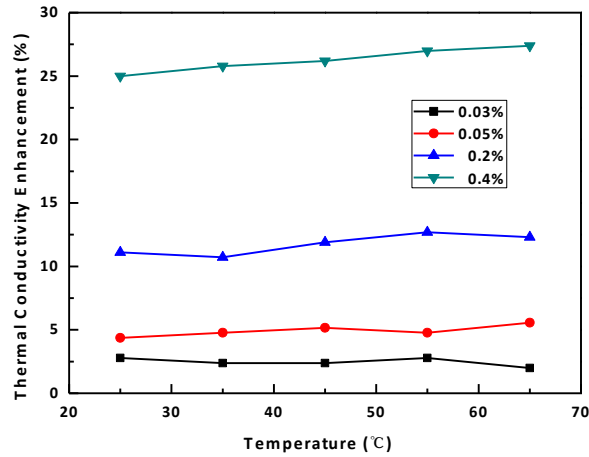


Figure 7. Thermal conductivity enhancement of graphite suspension as a function of temperature, showing that the enhancement is independent of temperature. Thermal conductivity enhancement is defined as (thermal conductivity of graphite suspension - thermal conductivity of solvent) / thermal conductivity of solvent.

It is also found that the effects of temperature on the thermal conductivity and viscosity of suspensions are quite different. As shown in Fig. 7, when the temperature varies from room temperature to 65 °C, the thermal conductivity enhancement does not vary significantly. This is consistent with the conclusion that Brownian motion is not responsible for the observed thermal conductivity enhancement in nanofluids⁸.

The effect of temperature on the viscosity of nanofluids and suspensions, however, is more complex than on the thermal conductivity. Fig. 8 a-c show the viscosity of several graphite suspensions as a function of shear rate at different temperatures. As the temperature increases from room temperature to 65 °C, the viscosity of dilute suspensions (less than 0.07 vol. %), which shows Newtonian behavior, is significantly reduced (Fig. 8a and b). Above the percolation threshold (higher than 0.07 vol. %), the results are more complex, and the variation with temperature is non-monotonic (Fig. 8c). We explore this complex thermo-rheological response in greater detail in Fig. 9.

Fig. 9 a-f plot the data to clearly show the temperature dependence of viscosity at different volume fractions and shear rates. For dilute suspensions (volume fraction less than 0.07%), the viscosity decreases with increasing temperature within the measured shear rate range (Figs. 9 a-c), similar to that of the pure solvent. At low shear rates, the viscosity depends strongly not only on temperature, but also on the volume fraction (Fig. 9 a). However, at higher shear rates, the difference of viscosity among different volume loadings becomes small (Fig. 9 b and c). For concentrated suspensions, more interesting phenomenon appears (Fig. 9 d-f). The viscosity increases with increasing temperature (Fig. 9d) at low shear rates but change to the opposite behavior at high shear rates (Fig. 9f).

The different effects of temperature on thermal conductivity and viscosity of nanofluids and suspensions indicate that Brownian motion is not important for thermal conductivity enhancement of nanofluids, but it is critical to the evolution of viscosity.

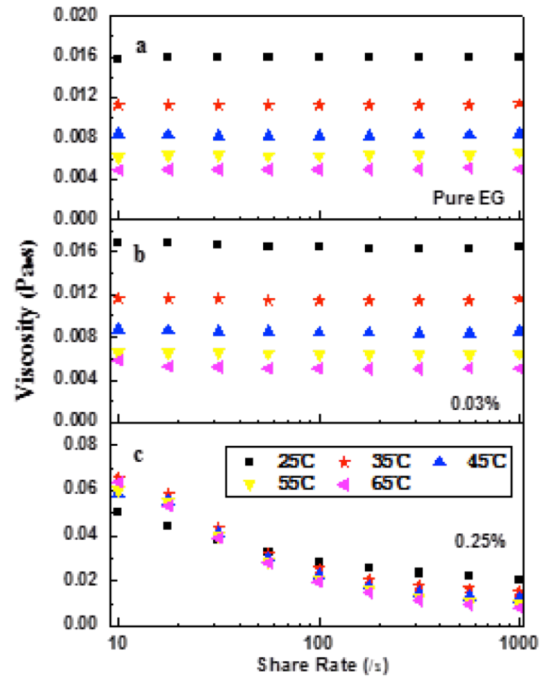


Figure 8. Viscosity of graphite suspensions as a function of shear rate at different temperatures and different loadings. (a) pure ethylene glycol(EG); (b) graphite–ethylene glycol suspension with 0.03 vol% graphite loading; (c) graphite–ethylene glycol suspension with 0.25 vol% graphite loading.

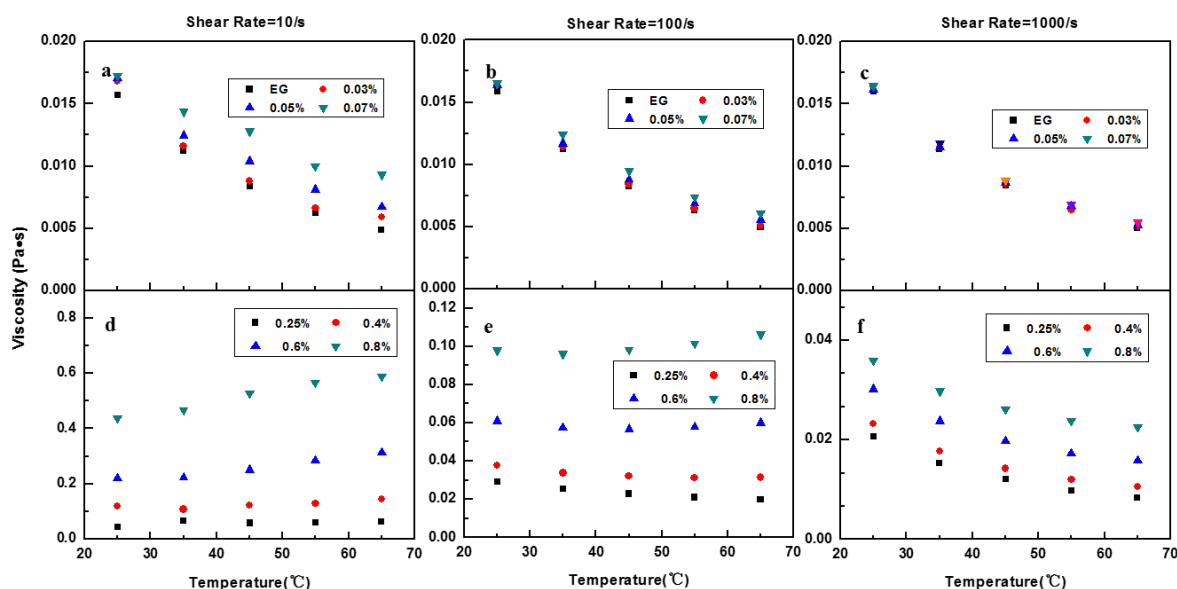


Figure 9: Viscosity as a function of temperature at different graphite volume fractions; (a)-(c) below percolation threshold, and (d)-(f) above percolation threshold. The temperature dependence of viscosity change trends above percolation threshold from low shear rates to high shear rates.

1.4 Summary

In this project, we have studied the effect of conductive phase, host materials and temperature on the physical properties of nanofluids (electrical and thermal conductivity, viscosity). It is found that with carbon nanotubes we can show up to 10^5 times change in electrical conductivity and three times in thermal conductivity during phase transition. We also found that ethylene carbonate is a better host matrix than alkanes regarding to high contrast in electrical and thermal conductivity during phase transition. Interesting behavior of temperature –dependent viscosity in nanofluids is investigated too.

2. Development of nanocomposites with temperature-regulated optical properties

Besides thermal regulation of thermal and electrical conductivity, it is also important to realize thermal regulation of optical properties, which has potential applications in smart roof/window technology, and low power optical sensors. The ability to control optical properties with temperature offers several distinct advantages over alternative approaches using electrical or mechanical actuation. First, device architecture is greatly simplified since external systems such as electronics, wiring, or mechanical pumps would not be needed. Second, these devices do not require an external power source in order to switch optical properties. Last and not least, these devices are inherently passive allowing for a fully automated system which dynamically responds to local changes in environment temperature.

To demonstrate the potential of this approach, we have developed two designs that incorporate phase change materials whose optical properties dramatically change at the phase transition. The first design utilizes gallium (Ga) in a nanocomposite whose optical properties change uniformly in the broad visible wavelength range. The second design uses vanadium oxide (VO_2) in a multilayer geometry which yields a narrowband response in the infrared (IR) wavelength range that shifts with temperature.

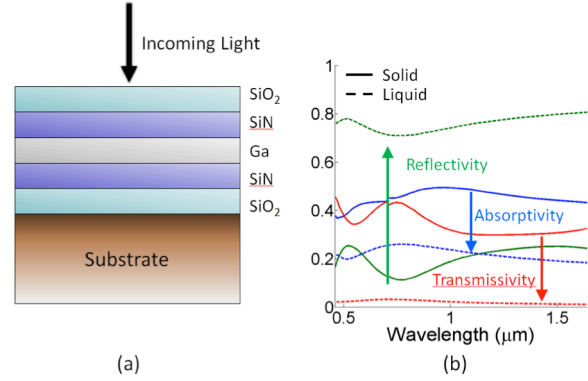


Figure 10. (a) Schematic of design. (b) Predicted optical properties showing a large contrast in reflectivity between solid and liquid Ga phases.

Ga is a unique metal that exhibits a solid to liquid melting point near room temperature of $T_m = 30^\circ\text{C}$. Although Ga remains a metal in both solid and liquid phases, its metastable α -crystalline phase shows significantly different optical properties compared to its liquid phase. For bulk Ga, past studies demonstrated a broad change in reflectivity of $\sim 20\%$, which is large for a bulk metal.⁹ Furthermore, alloying Ga with other metals, such as tin or indium, can shift the melting point even lower.

In order to increase the contrast in reflectivity even further, it was observed that the optical penetration depth of light for Ga is distinctly different between the solid and liquid phases. By using a thin-film of Ga with a thickness in between these length scales, transmission losses were introduced in the solid phase, but not the liquid phase, which is then captured by an underlying absorbing substrate. In this manner, the contrast in reflectivity between the solid and liquid phases can be larger. Figure 10a shows the design of the structure. The SiO_2 and SiN_x layers provide encapsulation for the Ga film.

Using a simple transfer-matrix approach, the optical properties of this nanocomposite were computed assuming no substrate present and normally incident light. The results are shown in Fig. 10b where the transmissivity is significant at $\sim 40\%$ in the solid phase, but negligible in the liquid phase. As a result, the change in reflectivity increases to $\sim 60\%$ across the entire visible and near-IR wavelength range. Further calculations showed that this contrast remains up to an angle of incidence of 60° . Therefore, this design would be well suited for smart roofing applications in order to dynamically reflect and absorb incoming sunlight during summer and winter seasons.

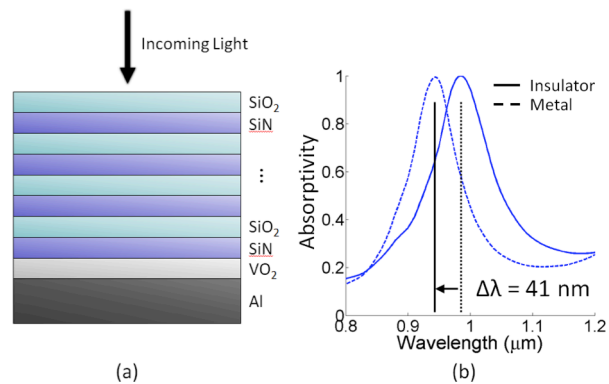


Figure 11. (a) Schematic of design. (b) Predicted optical properties showing large shift in peak absorptivity between insulating and metallic VO_2 phases.

At present, we are in the process of developing an experimental demonstration of this concept. The structure will be fabricated in a cleanroom facility using plasma enhanced chemical vapor deposition (PECVD) and e-beam evaporation tools. Morphological characterization of the structure will be achieved using a combination of x-ray diffraction spectroscopy (XRD), x-ray photoelectron spectroscopy (XPS), and scanning electron microscope (SEM) imaging. To measure its spectral properties, we will use standard UV-visible wavelength spectroscopy tools.

For the second design, VO_2 is a well-known material which exhibits a solid-to-solid insulator-to-metal transition at a temperature of $T_m = 68^\circ\text{C}$. Like Ga, VO_2 can be alloyed with other materials, such as tungsten, in order to decrease the phase transition temperature to near room temperature. For this reason, VO_2 has often been cited as an ideal material for IR smart windows.

To create a spectrally narrowband optical response, we drew inspiration from the field of plasmonics in which surface plasmon polaritons (SPPs) have been widely lauded for its potential in sensing applications. However, the key drawback in using SPPs is the inherent difficulty in coupling light to these modes due to the high momentum required for excitation. To overcome this limitation, our design consists of placing a Bragg reflector onto a metal. By itself, the Bragg reflector strongly reflects light via destructive interference. However, by placing a metal on the backside, a resonant surface mode, known as a Tamm state, is formed in which incident light can be strongly absorbed.² Unlike SPPs, light can easily couple to Tamm states even when illuminating at normal incidence.

The design for this structure, as shown in Fig. 11a, consists of a Bragg reflector, composed of silicon dioxide and silicon nitride, and aluminum. To actuate the spectral response with temperature, a thin-film of VO_2 is placed between the Bragg reflector and the metal in order to perturb the Tamm state.

Once again, a transfer-matrix approach is used to analyze the optical properties of this structure. As shown in Fig. 11b, the structure supports a narrowband peak in absorption centered at a wavelength of 985 nm when VO_2 is in its insulating phase. When VO_2 transitions to its metallic phase at high temperatures, this peak shifts by 41 nm to a wavelength of 944 nm. For comparison, optical fibers containing a Bragg grating have been used to sense temperature via a shift in reflectivity that is caused by thermal expansion of the grating's constituent layers. In these devices, the shift in wavelength is typically ~ 1 nm. Therefore, the predicted shift is significantly larger and holds promise in use in sensing applications.

3. Thermal regulation of phase transition for efficient steam generation

Besides using phase transition to control thermal transport and physical properties, we also develop methods to regulate thermal transport to control phase transition. By carefully controlling heat transfer in aqueous system, we efficiently convert sunlight energy to high temperature steam, which is a key factor for a broad range of applications, from

large-scale power generation, absorption chillers, and desalination systems to compact applications such as water purification for drinking, sterilization, and hygiene systems in remote areas.

Current methods of steam generation rely on a surface or cavity to absorb the solar radiation, and transferring heat to the bulk liquid directly or via an intermediate carrier fluid, which require high optical concentration and suffer from high optical loss and surface heat loss^{10, 11}. The steam thus generated is usually in thermal equilibrium with the bulk liquid. Our new approach and corresponding material structure localize the solar energy where evaporation occurs and minimizes the heat losses leading to enhanced solar-thermal efficiency at low optical concentration in open air while generating steam⁵. As shown in Fig. 12a, under solar illumination, the developed structure forms a hot spot internally where evaporation occurs. The fluid wicks to the hot spot, evaporates and forms vapor which leaves the structure. This structure needs to have four main characteristics: high absorption in the solar spectrum, low thermal conductivity to suppress thermal conduction away from the hot internal region, hydrophilic surfaces to leverage capillary forces and promote fluid flow to the hot region, and interconnected pores for fluid flow to and from the structure.

For the first demonstration of this approach, we developed a double layer structure (DLS) consisting of a carbon foam layer supporting an exfoliated graphite layer (Fig. 12b and c). The bottom carbon foam is thermally insulating with smaller pore size for liquid supply and the top exfoliated graphite layer has larger pore size for vapor escape. The reflectivity of the exfoliated graphite is measured with a spectrophotometer equipped with an integrating sphere and it is <3 % in the solar spectrum (250-2250 nm). Thus, 97% of the

irradiated solar power is absorbed within the top exfoliated graphite layer. The surface area of the exfoliated graphite layer is measured by N₂ adsorption to be approximately 320 m²g⁻¹, 32 times higher than graphite flakes for more efficient heat transfer to the fluid.

The evaporation rates of water with the DLS and the single exfoliated graphite layer (volumetric absorber) are measured by recording the weight change as a function of time and results are compared with pure water under solar illumination of 1 and 10 kWm⁻²,

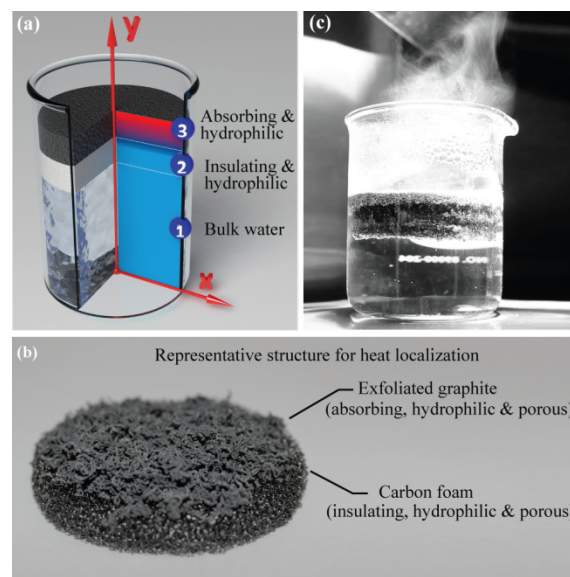


Figure 12: Double layer structure (a) A representative structure for localization of heat; the cross section of structure and temperature distribution (b) The DLS that consists of a carbon foam (10 mm thick) supporting an exfoliated graphite layer (~5 mm thick). Both layers are hydrophilic to promote the capillary rise of water to the surface (c) A picture of enhanced steam generation by the DLS structure under the solar illumination of 10 kWm⁻².

Fig. 13a and b. After an initial transient period, the evaporation rate reaches a constant value. At each optical concentration, an experiment was run for a long illumination time (more than 5 hours) and no change in evaporation rate is observed after the initial transient period. For pure water, the absorptance is small in the visible range. However, this small absorptance together with the larger absorptance in the infrared regime (not directly measured in this work) throughout the volume of the water causes an approximately 10 °C temperature rise in steady state condition under a solar intensity of 1 kWm⁻². This temperature rise leads to enhanced evaporation (~6 times) compared to a dark environment. The water evaporation rate in a dark environment is 74 g m⁻² hr⁻¹. This “dark” evaporation rate is subtracted from all the measured evaporation rates under the solar illumination to isolate the effect of solar irradiation on the evaporation rate. The DLS structure shows the highest evaporation rate and it is 2.1 and 2.4 times higher than pure water at 1 and 10 kWm⁻² solar illumination, respectively. To show the effect of the bottom layer of the DLS, if only exfoliated graphite (volumetric absorber) is utilized, the evaporation rate drops by 17% due to heat losses by conduction to the underlying water.

The thermal efficiency (η_{th}) is considered to assess the performance of DLS and is defined as

$$\eta_{th} = \frac{\dot{m} h_{LV}}{C_{opt} q_i} \quad (1)$$

where \dot{m} denotes the mass flux, h_{LV} total enthalpy of liquid-vapor phase change (sensible heat+ phase-change enthalpy), C_{opt} the optical concentration, and q_i the nominal direct solar irradiation 1 kWm⁻². The η_{th} of the DLS is an increasing function of optical concentration and goes from 64% at 1 kWm⁻² to 85 % at 10 kWm⁻², Fig. 2c. We emphasize that optical concentration losses are not considered in this analysis. Note that this level of optical concentration can be achieved by simple non-imaging optics with monthly adjustment without a tracking system, which reduce the overall cost of the system. We calculate the conduction losses to the underlying water. This loss at 10 kWm⁻² is 5±0.5 % of the total solar irradiation. The measured surface temperature of the exfoliated graphite is ~5 °C less than the generated vapor temperature. Considering emissivity of 0.97, under solar illumination of 10 kWm⁻², the radiation losses at the surface are 6 %. At a solar irradiation of 1 kWm⁻², the fraction of losses is ~35% (reflection~3%, conduction ~6%, surface radiation ~12%, test chamber parasitic losses ~14%). These losses are a decreasing function of solar irradiation, and the total loss drops to ~15% at 10 kw m⁻². If the steam is generated with the DLS at higher concentrations, we expect that efficiencies of more than 90 % is achievable. Here, we focused on low optical concentration to reduce the complexity and cost of solar harvesting system.

The evaporation rate as a function of optical concentrations is also shown in Fig. 13c. Localized energy close to the surface of the structure accompanied by a limited flow rate of fluid leads to an enhanced temperature of the generated vapor phase. At 10 kWm⁻², while steam is generated, the underlying liquid is close to ambient temperature as shown in Fig. 13d. This non-equilibrium process offers localized phase-change while the surrounding

medium remains cold. This localization leads to a significant drop in thermal losses by the bulk fluid and consequently a boost in the thermal efficiency of solar-thermal conversion.

In summary, we have developed an approach and corresponding material structure, the DLS, which simultaneously absorbs solar illumination, and confines the thermal energy (formation of hot spot) to near the structure surface while efficiently wicking the fluid to this hot spot. This structure yields a solar-thermal conversion efficiency of 85% at 10 kWm^{-2} solar illumination, while generating superheated vapor. Localization of heat is achieved by the broad-spectrum absorbing and thermally insulating properties of the DLS while the fluid flow is channeled to the hot spot by the hydrophilic and porous nature of the DLS. This work opens a new approach for solar assisted steam generation for many potential applications including power generation, desalination, waste water treatment, and hygiene systems.

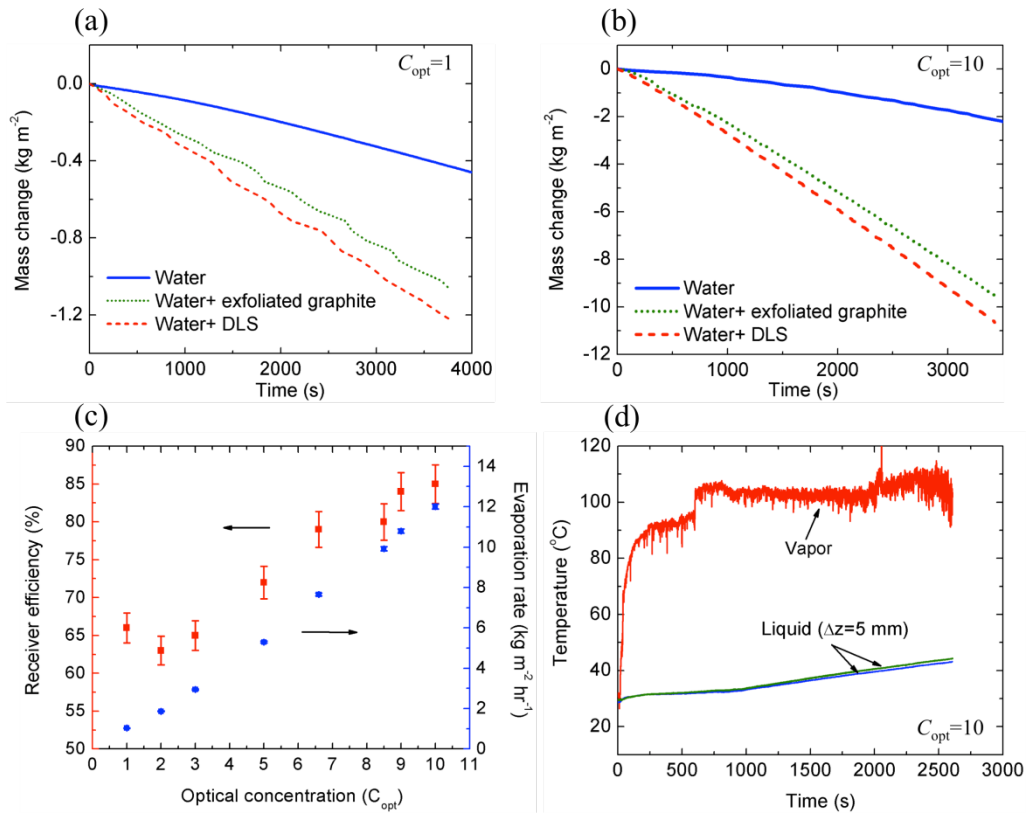


Figure 13. The evaporation mass loss of water with different structures under (a) 1 kWm^{-2} and (b) 10 kWm^{-2} solar irradiation is compared with the case of pure water. All experiments are conducted in ambient temperature of 24°C and the humidity of 31%. (c) The solar-thermal efficiency of the evaporation process by the DLS under a range of optical concentrations (left-hand side axis) and the corresponding evaporation rate (right-hand side axis). (d) While the steam is generated, the underlying bulk liquid is at the ambient temperature.

4. Electrochemical regulation of thermal conductivity in battery materials

In addition to thermal regulation, we also explored means to regulate thermal transport using electronic field and ionic transport. One example is to use intercalation of ions into materials to reversible control thermal conductivity that is typical in a battery operation. We used the intercalation of Li_xCoO_2 as a test material, and measured the thermal conductivity changes of the material when intercalated at different voltage and cycling thermal property change as lithium is driven in and out of the material. Good thermal property contrasts and cycling properties are observed, as shown in Fig. 14. These experiments show the promise of using intercalation compounds as solid-state thermal switches.

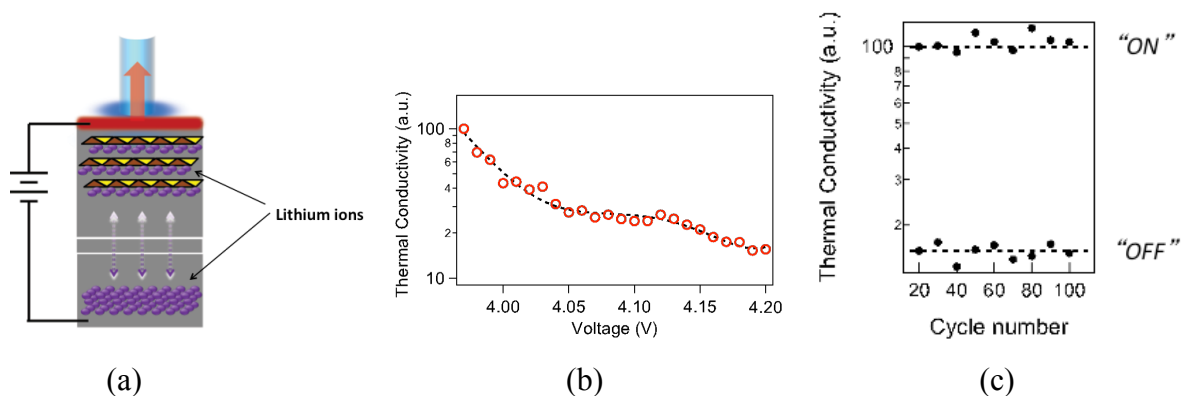


Figure 14 (a) Structure used to measure thermal conductivity of Li_xCoO_2 under different voltage, (b) measured thermal conductivity change under different voltage, and (c) cycling characteristics of the thermal properties.

5. Summary

In the past three years, we have developed significant scientific understanding on tuning thermal, electrical, and optical properties of materials. We also designed and demonstrated materials and devices to thermally regulate various transport processes including: 1) thermal regulation of electrical and thermal conductivity in phase transition of nanofluids, 2) thermal regulation of optical properties in multilayer thin film, and 3) thermal regulation of phase transition for efficient steam generation. We also develop electrochemical regulation of thermal conductivity in battery materials, which opens new direction for exploration. Both experiments and modeling have been carried out in to advance the fundamental understanding of transport processes during switching of thermophysical properties. Our results significantly advance understanding and capability to control physical properties. We highly appreciate the generous support from AFOSR.

6. Personnel Supported

Vazrik Chiloyan (PhD student)

Lei Ma (visiting student)

Zhiting Tian, (PhD student, now assistant professor at Virginia Tech)

Jonathan Tong (PhD student)

James (Jianjian) Wang (PhD student)

Jenny Wang (PhD student)

Dr. Jinwei Gao (Visiting student, now associate Professor at South China Normal University)

Dr. Hadi Ghasemi (supported by a NSERC fellowship, now assistant professor at University of Houston)

Dr. Yongjie Hu (supported by a Battelle fellowship, now assistant professor at UCLA)

Dr. Xiaopeng Huang (postdoc)

Dr. Amy Marconnet (postdoc, now assistant professor at Purdue University)

Dr. Bo Qiu, (postdoc)

Dr. Yuan Yang (postdoc)

Dr. Ruiting Zheng (visiting scholar, Professor at Beijing Normal University)

Prof. Gang Chen (principal investigator, 17% Aug. 2012, 8.25% Jun 2013)

7. Publications

1. R.T. Zheng, J.W. Gao, J.J. Wang, H.P. Feng, H. Ohtani, Jinbo Wang, and G. Chen, Thermal Percolation in Stable Graphite Suspensions, *Nano Letters*, 12(1), 188-192 (2012).
2. J. J. Wang, R. T. Zheng, J. W. Gao, and G. Chen, Heat Conduction Mechanisms in Nanofluids and Suspensions, *Nano Today*, 7, 124-136 (2012).
3. P. C. Sun, Y. L. Wu, J. W. Gao, G.A. Cheng, G. Chen and R. T. Zheng, Room Temperature Electrical and Thermal Switching CNTs/hexadecane Composites, *Advanced Materials*, 25(35), 4938-4943 (2013).
4. T. Luo and G. Chen, Nanoscale Heat Transfer---From Computation to Experiment, *Journal of Physical Chemistry and Chemical Physics* (invited review), 15, 3389-3412 (2013).
5. S.W. Lee, Y. Yang, H.W. Lee, H. Ghasemi, D. Kraemer, G. Chen, Y. Cui, An electrochemical system for highly efficient harvesting of low-grade heat energy, *Nature Communications*, 5, 3942 (2014).
6. H. Ghasemi, G. Ni, A.M. Marconnet, J. Loomis, S. Yerci, N. Miljkovic and G. Chen, Solar Steam Generation by Heat Localization, *Nature Communications*, 5, 4449 (2014).
7. Y. Bai, R. T. Zheng, Q. Gu, J. J. Wang, B. S. Wang, G. A. Cheng, and G. Chen, One-step synthesis of hollow $\text{Cr}(\text{OH})_3$ micro/nano hexagonal pellets and the catalysis properties of hollow Cr_2O_3 structure, *Journal of Materials Chemistry A*, 2, 12270-12775 (2014). 12770-12775

8. Y. Yang, S. W. Lee, H. Ghasemi, J. Loomis, X. B. Li, D. Kraemer, G. Y. Zheng, Y. Cui and G. Chen, A Charging-free Electrochemical System for Harvesting Low-grade Thermal Energy, submitted.
9. Lei Ma*, Jianjian Wang*, Amy M. Marconnet, Alexander C. Barbati, Gareth H. McKinley, Wei Liu and Gang Chen, Viscosity and Thermal Conductivity of Stable Graphite Suspensions Near Percolation, submitted. (* equal contribution)

8. Patents:

1. H. Ghasemi, A.M. Marconnet, and G. Chen, Localized Solar Collectors, US Patent Application No. 61/874390.
2. S. W. Lee, Y. Yang, H. Ghasemi, G. Chen and Y. Cui, Electrochemical systems and methods for harvesting heat energy. US Patent Application No. 14/308,669

9. Conference Presentations

1. J.J. Wang, R.T. Zheng, J.W. Gao, and Gang Chen, "Heat Conduction Mechanisms and Applications of Graphite Suspensions," Keynote at Carbon Nano Materials and Applications Workshop, Rapid City, SD, Oct. 30-Nov. 1, 2011.
2. G. Chen, "Nanoengineered Materials for Thermal Energy Systems," Plenary Lecture at International Mechanical Engineering Congress and Exhibition, Denver, Colorado, November 11-17, 2011.
3. G. Chen, "Extraordinary Heat Transfer at Nanoscale," Keynote at ASME 2012 3rd Micro/Nanoscale Heat and Mass Transfer International Conference, Georgia, Atlanta, March 3-6, 2012.
4. J.J. Wang, R.T. Zheng, J.W. Gao, and Gang Chen, "Heat Conduction in Nanofluids: Mechanisms and New Phenomena," Invited talk at *7th US-Japan Joint Seminar on Nanoscale Transport Phenomena*, Shima, Japan, December 11-14, 2011.
5. G. Chen, "Thermal Transport and Properties in Nanostructured Materials," 18th Symposium on Thermophysical Properties, Boulder, Colorado, June 24-29, 2012.
6. A.M. Marconnet, L. Ma, and G. Chen, "Impact of Phase Change on Thermal and Electrical Properties of Ionic Nanofluids" in *ASME Summer Heat Transfer Conference*, Minneapolis, MN, 2013.
7. G. Chen, "Thermal Transport in Soft Matters: Polymers and Nanofluids," (Invited talk), *Organic Electronics and Transport Phenomena*, Max Planck Institute for Polymer Research, Mainz, Germany June 10 - 12, 2013.
8. L. Ma, J.J. Wang, A. Marconnet, G. Chen, "Viscosity and thermal conductivity of stable graphite suspension near percolation," *The 4th International Symposium on Micro and Nano Technology*, Shanghai, China, 2013.

9. G. Chen, "Nanoscale Heat Transfer for Energy Applications," Keynote at 3rd *International Forum on Heat Transfer*, Nagasaki, Japan, November 11-15, 2012.
10. G. Chen, "Heat Transfer at Intersections," Keynote Lecture at ASME 2013 Summer Heat Transfer Conference, Minneapolis, MN, July 14-19, 2013.
11. G. Chen, "Heat Transfer at Interfaces," Nukiyama Memorial Award Lecture, International Heat Transfer Conference, Kyoto, Japan, August 10-15, 2014.

References:

1. Zheng, R.; Gao, J.; Wang, J.; Chen, G. *Nature Communications* **2011**, 2.
2. Sun, P. C.; Wu, Y. L.; Gao, J. W.; Cheng, G. A.; Chen, G.; Zheng, R. T. *Advanced Materials* **2013**, 25, (35), 4938-4943.
3. Kole, M.; Dey, T. K. *Journal of Applied Physics* **2013**, 113, (8).
4. Hojjat, M.; Etemad, S. G.; Bagheri, R.; Thibault, J. *International Communications in Heat and Mass Transfer* **2011**, 38, (2), 144-148.
5. Ghasemi, H.; Ni, G.; Marconnet, A. M.; Loomis, J.; Yerci, S.; Miljkovic, N.; Chen, G. *Nature communications* **2014**, 5, 4449-4449.
6. Osuji, C. O.; Kim, C.; Weitz, D. A. *Physical Review E* **2008**, 77, (6).
7. Ma, L.; Wang, J.; Chen, G. **submitted**
8. Wang, J. J.; Zheng, R. T.; Gao, J. W.; Chen, G. *Nano Today* **2012**, 7, (2), 124-136.
9. Albanis, V. Light-Induced Structural Transition and Reflectivity of a Silica-Gallium Interface. University of Southampton, 2003.
10. Lenert, A.; Wang, E. N. *Solar Energy* **2012**, 86, (1), 253-265.
11. Fend, T.; Hoffschmidt, B.; Pitz-Paal, R.; Reutter, O.; Rietbrock, P. *Energy* **2004**, 29, (5-6), 823-833.